Combustion and Flame 254 (2023) 112850

Contents lists available at ScienceDirect

Combustion and Flame

journal homepage: www.elsevier.com/locate/combustflame

# On-line monitoring of carbon nanostructure and soot reactivity in engine exhaust by dual-pulse laser-induced incandescence

Fabian P. Hagen[a,b,*], Daniel Kretzler[a], Sergej Koch[c], Henning Bockhorn[a], Rainer Suntz[b], Dimosthenis Trimis[a], Heiko Kubach[c], Amin Velji[c], Thomas Koch[c]

[a] Karlsruhe Institute of Technology (KIT), Engler-Bunte-Institute, Combustion Technology, Karlsruhe, Germany
[b] Karlsruhe Institute of Technology (KIT), Institute of Chemical Technology and Polymer Chemistry, Karlsruhe, Germany
[c] Karlsruhe Institute of Technology (KIT), Institute of Internal Combustion Engines, Karlsruhe, Germany

ARTICLE INFO

*Article history:*
Received 13 February 2023
Revised 13 May 2023
Accepted 14 May 2023
Available online 1 June 2023

*Keywords:*
Soot nanoparticles
Gasoline direct injection engine
Laser-induced incandescence
Carbon nanostructure
Soot oxidation
Gasoline particulate filter

ABSTRACT

In previous work, we introduced the dual-pulse two-color time-resolved laser-induced incandescence (DP-2C-TiRe-LII), which is possibly suitable for on-line monitoring of the nanostructural topology of inhomogeneous soot particle ensembles in transient flows. The method relies on the quantitative relationship between the size of the basic structural units (BSUs) embedded within primary particles and the ratio of the refractive-index function for absorption at two wavelengths $E(m,\lambda_{UV})/E(m,\lambda_{NIR})$. As the size of BSUs increases, the band gap energy for an electronic $\pi \rightarrow \pi^*$ transition becomes narrower increasing the wavelength for absorption and, hence, forcing $E(m,\lambda_{UV})/E(m,\lambda_{NIR})$ to decrease. Once quantitative correlations between the carbon nanostructure, i.e., size of the BSUs, and a structure-associated particle property are available, its on-line monitoring becomes accessible through monitoring of $E(m,\lambda_{UV})/E(m,\lambda_{NIR})$. The objective of this paper is to provide the proof-of-concept for on-line monitoring of an exemplary structure-associated particle property, viz. soot reactivity against oxidation, in an application from practice. For this, DP-2C-TiRe-LII is employed downstream of a gasoline direct injection (GDI) engine running under steady-state and transient operating conditions. Intrusive particle sampling in combination with an analytical toolbox comprising high-resolution transmission electron microscopy (HRTEM), pattern recognition methods, elemental analysis (EA), and thermogravimetric analysis (TGA) was applied to validate the results from DP-2C-TiRe-LII. Excellent agreement is found between particle properties derived via ex situ and in situ diagnostics. Moreover, the transformation of the time series of $E(m,\lambda_{UV})/E(m,\lambda_{NIR})$ into probability density distributions seems to represent the BSU size distributions of the investigated soot particle ensembles. Likewise, soot reactivity is reflected in the distributions of $E(m,\lambda_{UV})/E(m,\lambda_{NIR})$.



## 1. Introduction

Soot nanoparticles emitted from practical combustion devices have significant impact on our daily lives. On the one hand, they are well-known air pollutants that adversely affect cardiovascular and pulmonary health and, in conjunction with volatile organic compounds (VOCs) adsorbed on their surface, are suspected of being carcinogenic [1,2]. On the other hand, soot nanoparticles contribute to global warming through direct radiative forcing [3,4], reduce the albedo of snow and ice surfaces [5], and significantly affect cloud formation processes [5,6]. Bond et al. concluded that carbonaceous particles are the second largest contributor to global warming after $CO_2$ with a radiative forcing of +1.1 W/m$^2$ [7].

Internal combustion engines (ICEs) constitute a major emission source for soot nanoparticles. The inevitable soot formation in ICEs results from incomplete combustion of hydrocarbons [8]. Incomplete conversion of the fuel molecules in fuel-rich zones inside the cylinder, facilitates soot formation from precursor molecules via particle inception, particle growth by reactions with gaseous components, coagulation, carbonization and (partial) oxidation [9–11]. The generated soot consists of sphere-like primary particles with sizes $d_P$ ranging from 10 nm to 50 nm and size distributions approximated best by log-normal size distributions [12–16]. The spheres coagulate into branched-chain, fractal-like aggregates

* Corresponding author at: Karlsruhe Institute of Technology (KIT), Engler-Bunte-Ring 7, Karlsruhe 76131 Germany.
*E-mail address:* fabian.hagen@kit.edu (F.P. Hagen).

https://doi.org/10.1016/j.combustflame.2023.112850

[17,18]. Graphene-like basic structural units (BSUs) of varying size $L_f$, referred to as carbon nanostructure, build the structure of primary soot particles in the sub-nm range [19–23].

Particularly, for soot emitted from diesel (D) and gasoline direct-injection (GDI) engines, the application of exhaust gas aftertreatment systems is inevitable to comply with increasingly stringent international legislation concerning particulate emissions [24–27]. An effective method for reducing soot emissions from GDI and D engine powered vehicles is the implementation of particulate filters (PF) [27,28]. Detailed information on GDI particulate emissions, current emission regulations, and gasoline particulate filters (GPFs) is provided in the comprehensive review by Awad et al. [29]. Along with a filtration efficiency of 44 wt.% to 99 wt.% [30,31], a continuous loading of the PF is accompanied. The accumulated soot within the PF channels increases the exhaust backpressure and thus promotes combustion instabilities [28,32]. Although reactive soot nanoparticles are continuously oxidized with residual oxygen in the exhaust gas, an active regeneration process needs to be initiated when the maximum PF soot loading is reached. This is performed by raising the exhaust gas temperature by increasing fuel injection [29]. Required temperatures as well as reaction times for oxidation are determined by the reactivity of soot against oxidation by molecular oxygen as discussed in Hagen et al. [23]. The conversion kinetics of soot particles and their reactivity, respectively, can be measured by thermogravimetric analysis (TGA) [23,33–40] or temperature-programmed oxidation (TPO) [41–43]. Non-isothermal experiments enable the determination of kinetic parameters for a one-step reaction with Arrhenius-type of temperature dependence of the reaction rate, from which reactivity indices of a studied soot particle system may be derived [23,44].

Various hypotheses attempted to explain the different reactivity of engine generated soot depending on their formation conditions, e.g., combustion mode, pressure, fuel type and composition [32,34,36,37]. First, Vander Wal and Tomasek postulated the dependence of soot oxidation rate on the size $L_f$ and curvature of the graphene-like BSUs embedded in primary particles. They showed that the oxidation rates of differently synthesized soot particles, exhibiting different nanostructural properties, differ by more than 400 % [45]. This hypothesis was later quantified based on high-resolution transmission electron microscopy (HRTEM) studies combined with pattern recognition methods [22,23,37,44]. In ref. [44] correlations between the size $L_f$ of BSUs, a reactivity index *RI*, and $E(m,\lambda_i)/E(m,\lambda_j)$ have been worked out. Findings on nanostructural properties influencing soot reactivity have been confirmed using X-ray diffraction (XRD) [33] and Raman spectroscopy (RS) [22,23,37,41–43], which both yield integral information about the carbon nanostructure. Especially $L_f$ determines the number density of edge-site carbon atoms and C-H groups accessible for oxidation. The shorter $L_f$, the higher the share of edge-site carbon atoms and C-H groups that may be attacked by oxidative species, and, consequently, the higher the reactivity against oxidation [22,23,44,45]. Another explanatory approach considers the geometric particle properties as decisive for soot reactivity, especially the primary particle size $d_P$ and its distribution $P(d_P)$. Several authors, e.g., [33,34,41], found that small primary particle sizes correlate with high reactivity and vice versa. However, others [23,37] showed that different reactivities against oxidation are independent of or only slightly dependent on the primary particle diameter and its distribution. In [44], we presume a correlation between the count median diameter *CMD* of the primary particle size distribution $P(d_P)$ and the size of BSUs. This is substantiated by the possibility of embedding layers with increasing $L_f$ more likely in particles with increasing *CMD*.

Apart from nanostructural characteristics, catalytic-active agents incorporated into soot aggregates may also increase soot reactivity. Choi and Seong concluded that calcium compounds are the key driving factor for catalytic oxidation of GDI engine generated soot [35]. Other studies attributed potassium [46], iron [41], zinc [41,47], aluminum [47] or copper [41] compounds catalytic activity. Bensaid et al. concluded that ceria-based particles positively impact the oxidation behavior of soot particles [48]. However, it has recently been hypothesized that the addition of catalytic-active species reduces the size of graphene-like structures during particle formation [46]. The reactivity enhancement caused by these species, therefore, may also have its origin in carbon nanostructural properties.

Direct measurement of the conversion kinetics of soot oxidation via TGA and/or TPO involves time-consuming and non-trivial particle sampling in combination with ex situ experiments. Therefore, efforts have been made to develop in situ diagnostics to derive this quantity. One approach involved soot oxidation in a tubular flow reactor at constant temperature. The change in aggregate size distributions or mass concentration measured via a tandem differential mobility analyzer (TDMA) [49], differential mobility analyzer coupled with an aerosol particle mass analyzer (DMA-APM) [50] and photoacoustic (PA) spectroscopy [51] allowed conclusions about the reactivity of soot particles emitted by various sources. However, the temporal resolution of the referred techniques is not sufficient to resolve fast transient processes.

Therefore, an alternative approach based on correlations between $L_f$, the reactivity index *RI*, and $E(m,\lambda_i)/E(m,\lambda_j)$ has been proposed in Hagen et al. [44]. In [52] we introduced the dual-pulse two-color time-resolved laser-induced incandescence (DP-2C-TiRe-LII), which is suitable for measuring optical properties such as the ratio of the refractive-index function for absorption at two wavelengths $E(m,\lambda_i)/E(m,\lambda_j)$ as well as absolute $E(m,\lambda)$ of inhomogeneous soot particle ensembles in transient flows. Using this approach, a non-intrusive on-line monitoring of $L_f$ and of soot reactivity *RI* of engine generated soot particles may apparently be possible.

The objective of this paper is to employ DP-2C-TiRe-LII as a method for on-line monitoring of the optical properties of soot and thereby the carbon nanostructure as well as the reactivity of soot in a combustion application from practice. This is accomplished by applying the non-intrusive in situ diagnostics described in ref. [52] downstream of a gasoline direct injection (GDI) engine running under both, steady-state and transient operating conditions. Particle properties are verified with intrusive particle sampling and application of a comprehensive analytical ex situ quantification of carbon nanostructure and reactivity. The applied analytical toolbox comprises HRTEM in combination with pattern recognition methods, elemental analysis, and TGA. Section 3 presents the results of the comprehensive ex situ characterization of particles collected during the investigated engine operating points and the results of DP-2C-TiRe-LII. Section 4 summarizes the findings and provides some concluding remarks.

## 2. Materials and methods

### 2.1. Laser diagnostics

In previous work, Minutolo et al. [53], Jäger et al. [54] and Williams et al. [55] presumed an effect of the order, extension, and the orientation of basic structural units on the wavelength-dependent absorption of soot particles. This hypothesis was verified in Hagen et al. [44], deriving a quantitative relationship between the size of the basic structural units (BSUs) and the ratio of the refractive-index function for absorption at two wavelengths $E(m,\lambda_i)/E(m,\lambda_{NIR})$, where $\lambda_{NIR} = 1064$ nm and $\lambda_i = \lambda_{UV}$ with 266 nm and 355 nm or $\lambda_i = \lambda_{VIS} = 532$ nm. The correlation is found to be linear. The spectroscopic background is the optical band gap energy $E_{OG}$ for an electronic $\pi \rightarrow \pi^*$ transition,

which decreases with increasing size of the conjugated $\pi$ system. In turn, an increasingly narrow $E_{OG}$ increases light absorption in the near-infrared spectral range, causing $E(m,\lambda_i)/E(m,\lambda_{NIR})$ to decrease and vice versa. Since quantitative correlations between size of the basic structural units and soot reactivity have also been derived [23,44], its non-intrusive in situ monitoring becomes accessible through recording of $E(m,\lambda_i)/E(m,\lambda_{NIR})$.

In order to determine $E(m,\lambda_{UV})/E(m,\lambda_{NIR})$ from inhomogeneous aerosols and in transient flows, we introduced the DP-2C-TiRe-LII [52]. This approach involves irradiating a particle ensemble by two subsequent laser pulses of different wavelengths with a time delay long enough to ensure cooling of the particles after the first pulse, but short enough to prevent the particles from moving out of the probe volume. In the experiment, the first pulse at $\lambda_{UV}$ is kept at low and constant fluence, whereas the fluence of the second pulse at $\lambda_{NIR}$ is periodically modulated. If coincidence of the generated two TiRe-LII signal decays is repeatedly achieved, $E(m,\lambda_{UV})/E(m,\lambda_{NIR})$ can be evaluated. The computed ratios are corrected for scattering based on the Rayleigh–Debye–Gans theory for fractal aggregates (RDG-FA) using aggregate sizes measured in Koch et al. [36]. Details of this approach as well as a detailed discussion on the influence of scattered light on $E(m,\lambda_{UV})/E(m,\lambda_{NIR})$ are provided in ref. [52]. Moreover, effects of the selected fluence of the first pulse on carbon nanostructure and, therefore, $E(m,\lambda_{UV})/E(m,\lambda_{NIR})$ are worked out in Hagen et al. [52]. The findings are in good agreement with the double-pulse experiments of Török et al. [56].

The synchronous temperature determination of the laser-pulse heated particles even enables the quantification of the absolute values of $E(m,\lambda_{UV})$ and $E(m,\lambda_{NIR})$ [52,57]. The particle temperature after laser pulse heating is determined experimentally by the two-color method, employing Planck's radiation law. Details regarding this approach and its experimental methodology are provided in Hagen et al. [52], Schulz et al. [58], Michelsen et al. [59]. The TiRe-LII signal decay induced by a NIR laser pulse in the low-fluence regime ($f_{NIR} < 0.2$ J/cm$^2$ [58]), provides besides quantitative information about the optical properties also information about the size distribution of the primary soot particles $P(d_P)$, see e.g., the review articles by Schulz et al. [58] and/or Michelsen et al. [59], and references therein. The particle size distribution $P(d_P)$ is evaluated by a multidimensional nonlinear fit of the calculated size distributions to the measured TiRe-LII signals. From this, the count median diameter, *CMD*, and the geometric standard deviation, $\sigma_g$, can be determined. Details, equations, and assumptions of the employed model are provided in Hagen et al. [52], Lehre et al. [60], Charwath et al. [61].

Center part of the optical DP-2C-TiRe-LII setup are two 10 Hz pulsed Nd:YAG lasers. The near-infrared (NIR) laser operates at the fundamental frequency $\omega$ @$\lambda_{NIR} = 1064$ nm, while the ultraviolet (UV) laser operates at the third harmonics $3\omega$ @$\lambda_{UV} = 355$ nm. Applying the fourth harmonics $4\omega$ @$\lambda_{UV} = 266$ nm has not been realized in this work because the strong light absorption of soot particles at this wavelength generates strong TiRe-LII decay signals even at very low laser fluence $f_{UV}$. In contrast to this, soot particle ensembles emitted from the GDI engine absorb near-infrared laser light less strong and, therefore, generate only small TiRe-LII signals. As a consequence, the events with coincidence of the signals in the DP-2C-TiRe-LII experiments using the wavelength pair $\lambda_{UV} = 266$ nm and $\lambda_{NIR} = 1064$ nm are less frequent.

The first pulse of DP-2C-TiRe-LII is emitted by the UV laser, operating at a constant, low fluence of $f_{UV} = 0.02$ J/cm$^2$, continuously being recorded using a power meter. The second laser pulse emitted by the NIR laser is delayed by a time interval of $\Delta t = 2$ µs. The NIR laser beam passes through a rotating $\lambda/2$ plate with precisely controlled rotation speed. The subsequent polarization beam splitter reflects the s-polarized component into a beam dump while allowing the *p*-polarized component to pass through. Due to the continuous rotation of the $\lambda/2$ plate, the NIR laser fluence is periodically modulated. The single laser pulses are detected by the Rayleigh scattered light using a photodetector normal to the beam path. This procedure allows a pulse-to-pulse evaluation of the energy density for each of the modulated NIR laser pulses. The DP-2C-TiRe-LII signal decays were collected at 90° angle to the laser beam using a lens system and two photomultipliers equipped with narrow band-pass interference filters (10 nm FWHM) centered at ${\lambda_d}^{i} = 450$ nm and ${\lambda_d}^{ii} = 650$ nm. To avoid possible structural changes of the particles by laser pulse heating, the fluence of the UV laser has been limited to 0.02 J/cm$^2$ and that of the NIR laser to 0.2 J/cm$^2$ maximum, see discussion in ref. [52] and the literature cited therein.

A detailed description of the experimental arrangement with two Nd:YAG pulse lasers, beam shaping, combining and profiling optics as depicted in Fig. 1 as well as the DP-2C-TiRe-LII theory, an exploratory study of the method including validation experiments are provided in Hagen et al. [52].

### 2.2. GDI engine test rig

A turbocharged four-cylinder engine with gasoline direct fuel injection served as application from practice. As fuel gasoline with a Research Octane Number of $RON = 98$ as test fuel has been used. The GDI engine was operated in a transient cold-start cycle changing over into subsequent steady-state operation conditions. To minimize influences from lubricating oil on combustion, the engine tests were carried out with external crankcase ventilation and fresh lubricating oil. Technical data and specifications of the engine test rig and fuel are summarized in Koch et al. [32,36].

Figure 2 depicts the engine test rig including the applied measurement instrumentation. Soot particles are sampled downstream of the engine using a constant volume sampler (CVS) with a dilution ratio of $DR = 5$ [32,36]. The soot samples collected on quartz fiber filters are analyzed employing a toolbox of analytical methods described in Section 2.4. The laser beams of the DP-2C-TiRe-LII are introduced into the exhaust tract ~ 1.5 m downstream of the exhaust manifold via an optically accessible section. In addition, a type K thermocouple allows the continuous measurement of the exhaust gas temperature at this position. As shown in Fig. 2, the intrusive particle sampling as well as the optically accessible section are located upstream of the exhaust gas aftertreatment system involving a three-way catalytic converter (TWC) and a gasoline particulate filter (GPF).

The exhaust gas soot volume fractions $f_V$ during engine operation may be estimated using the correlation postulated by Northrop et al. [62], enabling a transformation of filter smoke numbers *FSN* given in Koch et al. [32,36] into mass concentrations. The necessary estimation of the soot density is given in Michelsen [63].

### 2.3. Engine operating points

In the experiment, the particles formed in a five-minute transient cold start period of the GDI engine were investigated. The GDI engine had a surface temperature of 283 K at the beginning of the experiment. Subsequently, the test conditions of the GDI test engine listed in Table 1 were attained in five-minute steady-state periods, with transitions occurring instantaneously.

The start of fuel injection *SOI* determines the time available for mixing and homogenization of fuel and oxidizer. Therefore, injection timing sets an essential parameter of mixture formation. The influence of *SOI* of the GDI engine investigated in this study on aggregate number density, size distribution, soot reactivity against oxidation, and inpact on the carbon nanostructure, was reported by

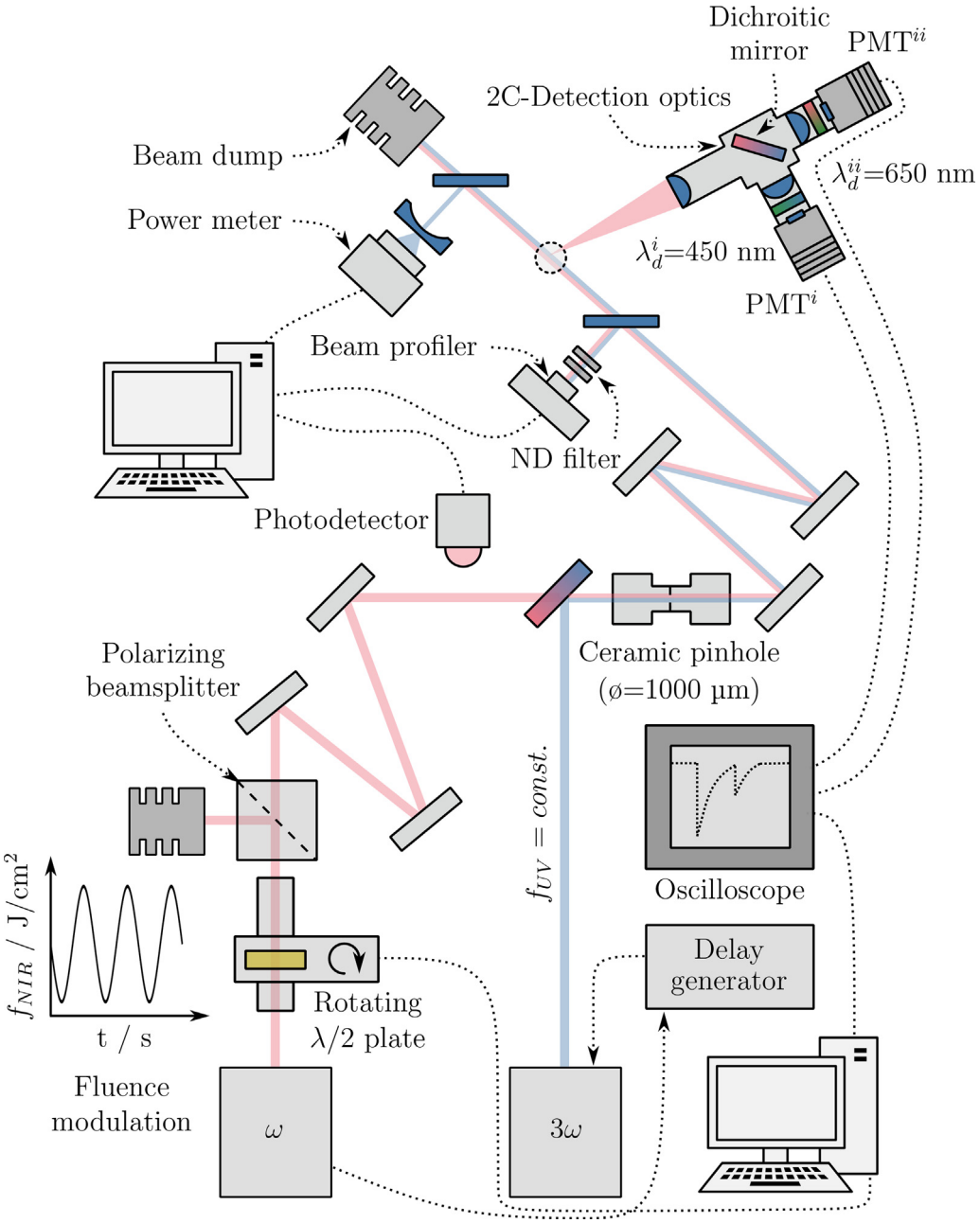


**Fig. 1.** Optical setup of DP-2C-TiRe-LII.

Koch et al. [36]. This *SOI* variation serves as the basis for the operating points (OPs) examined in this study, which are summarized in Table 1.

OP 0. is the transient cold start cycle. In the stationary OPs i. to v., the fuel was injected using a constant rail pressure of $P_r = 10^4$ kPa. The *SOI* was varied from 310 °CA, 280 °CA, 250 °CA to 220 °CA before top dead center (BTDC) at a constant ignition timing of 25 °CA BTDC. For simplicity, °CA BTDC is abbreviated as °CA in the following. *SOI* variations were performed at constant engine speed of $n = 2000$ rpm and a break mean effective pressure of $P_m = 800$ kPa. While in OP i. to iv. a stoichiometric mixture was used, the equivalence ratio $\Phi$ was decreased at OP v., $SOI = 220$ °CA. For more oxygen-rich conditions at $\Phi < 1.0$, the influence of an enhanced in-cylinder post-oxidation of formed soot nanoparticles on carbon nanostructure and reactivity can be analyzed. Finally, an OP presented in Koch et al. [32] was selected representing the least reactive particles which can be synthesized in the GDI engine. The formation of these non-reactive particles was achieved with a double injection at $SOI = 280$ °CA and 70 °CA, a reduction of the rail pressure, which is accompanied by a modified spray pattern, and a fuel rich combustion with $\Phi = 1.1$.

### 2.4. Analytical toolbox for the ex situ characterization of collected soot particles

Particles collected on quartz fiber filters from the particle-laden exhaust gas by CVS [32,36] are studied with a number of analytical methods described in the following sections.

#### 2.4.1. Thermogravimetric analysis

Soot reactivity against oxidation is ex situ analyzed employing TGA. Non-isothermal, dynamic experiments using a constant heating rate of $\beta = 5$ K/min and an oxygen concentration of 5 vol.%

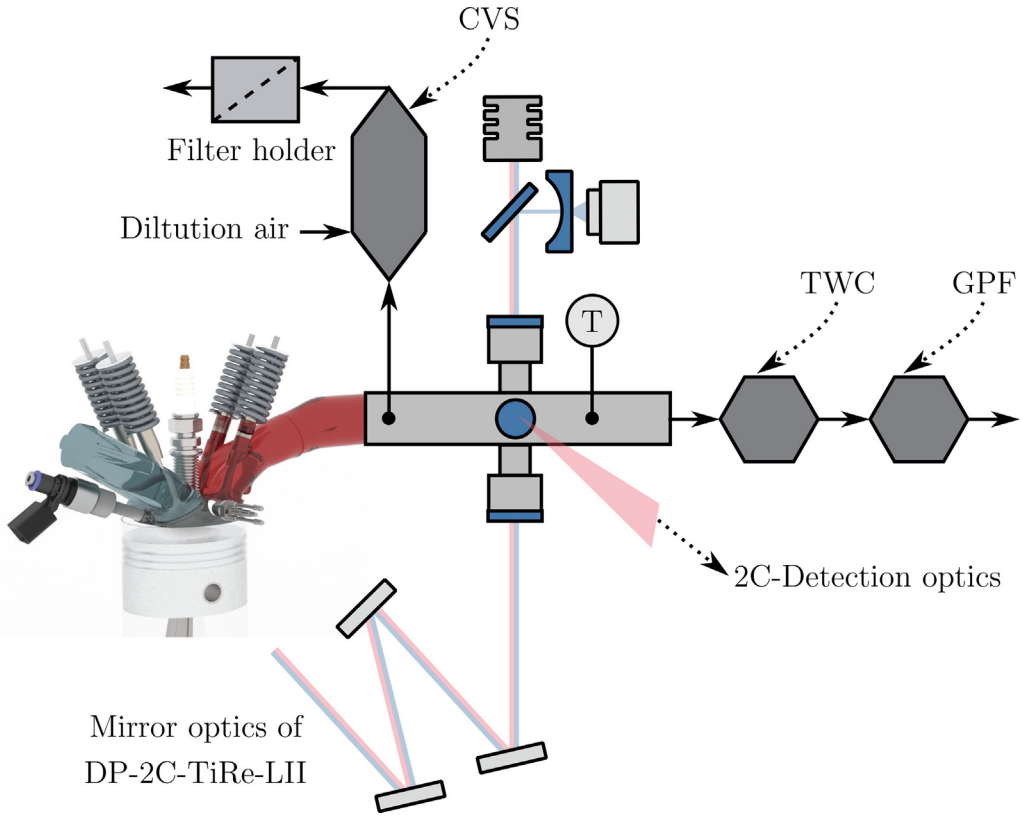


**Fig. 2.** Engine test rig for on-line monitoring of carbon nanostructure and reactivity of soot from GDI. The constant volume sampling (CVS) of engine exhaust gas is designed to collect engine generated particulate samples on quartz fiber filters for ex situ analysis. After the exhaust gas aerosol crosses the optical access, it passes through the three-way catalytic (TWC) converter and the gasoline particulate filter (GPF).

serve to quantify the conversion profile during soot oxidation. Details of the experimental procedure including the instrumentation are described elsewhere [23,44,64].

The experimental TGA conversion profiles are reproduced using a global, over-all kinetic expression [23,44]

$$\frac{d\alpha}{dT}\cdot\beta \;=\; r_{ox} = -k_{0,ox}\cdot\exp\left[-\frac{E_A}{\Re\, T}\right]\alpha^{n_{ox}}. \tag{1}$$

Here, $E_A$ is the apparent over-all activation energy, $n_{ox}$ the over-all order of reaction, $\beta$ the heating rate, and $\Re$ the universal gas constant. The dimensionless turnover parameter $\alpha$ relates the time-dependent mass loss to the initial particle mass: $\alpha = m(t)/m_0$. The pre-exponential factor $k_{0,ox}$ containes the oxygen concentration, which is assumed to be constant due to excess oxygen, and for $n_{ox} \neq 1$ the initial particle mass $m_0$.

Depending on the operation conditions, soot emitted from GDI engines can contain different fractions with different $E_A$ and, therefore, different reactivities [32,36]. The TGA oxidation profiles of such soot aggregates are described using a multiple reactants kinetic approach [64]. The oxidation rate of each reactant is defined according to Eq. (1) and the effective oxidation rate $r_{eff}$ can be described by Koch et al. [32], Hagen et al. [44]:

$$r_{eff} = \sum_{i=1}^{n} x_i\; r_{ox,i}. \tag{2}$$

Here, $x_i$ describes the mass fractions of the $n$ different reactive soot fractions. The experimentally determined conversion profiles are fitted using the global total kinetic expression according to Eqs. (1) and (2). A three educt approach, $i = 1\ldots3$, is applied in this study. The effective oxidation rate is employed to define a reactivity index *RI*. Following the IUPAC recommendations [65], the effective oxidation rate under specific reaction conditions is considered in this study. As suggested in Hagen et al. [44], *RI* considers $r_{eff}$ at $T = 800$ K, 5 vol.% $O_2$ and $\alpha = 0.5$. To cover a range of $0 \leq RI \leq 1$, the cumulative oxidation rate is normalized by the reaction rates of the maximum (max) and minimum (min) reactive soot particle system [32,44].

$$RI_i = \left[\frac{[\ln(r_{eff})]_{\min} - \;[\ln(r_{eff})]_i}{[\ln(r_{eff})]_{\min} - [\ln(r_{eff})]_{\max}}\right]_{T=800\text{ K},\ \alpha=0.5,\ 5\text{ vol.\% }O_2}. \tag{3}$$

### 2.4.2. High-resolution transmission electron microscopy

Carbon nanostructure and primary particle size distributions were analyzed using high-resolution transmission electron microscopy (HRTEM). HRTEM images were acquired using a Philips CM200 transmission electron microscope (ThermoFischer Scientific Inc.), operated at 200 kV resulting in highest spatial resolution of 0.0283 nm/px. The sample preparation was analogous to Koch et al. [32]. To evaluate the size distributions $P(L_f)$ of BSUs embedded within primary particles, a pattern recognition algorithm [23] was employed. In addition, the primary particle size distribution was also evaluated using the HRTEM images. Details are given in Hagen et al. [23] as well.

### 2.4.3. Elemental analysis

The elemental analysis (EA) serves to quantify the molar carbon-to-hydrogen ratio of the emitted particles. Carbon and hydrogen fractions of the soot particles emitted during the OPs, see Table 1, have been analyzed using a Vario Micro Cube elemental analyzer equipped with thermoconductivity (TCD) and infrared (IR) detectors. Further details are given in Hagen et al. [64].

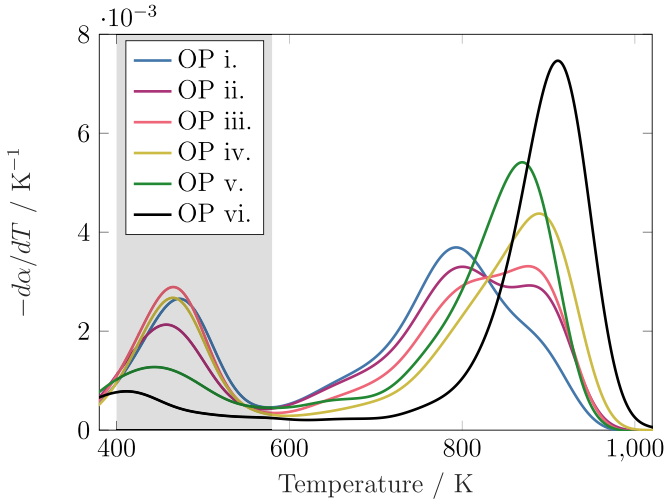


**Fig. 3.** TGA oxidation profiles of soot particles from the GDI engine for the OPs summarized in Table 1.

## 3. Results and discussion

### 3.1. Comprehensive ex situ characterization of GDI soot particles

Particle sampling via CVS and subsequent characterization via the methods described in Section 2.4 enables a comprehensive analytical quantification of the reactivity against oxidation, size distributions of BSUs, and primary particle size distributions.

#### 3.1.1. Soot reactivity via TGA

The experimentally determined TGA profiles $-d\alpha/dT$ of the soot samples collected during the six OPs listed in Table 1 are plotted in Fig. 3. All investigated engine generated soot samples exhibit a peak at $\sim 450$ K, which is associated with the desorption of volatile organic compounds (VOCs), as verified by coupling the TGA exhaust pipe with a quadrupole mass spectrometer (QMS) and/or Fourier-transform infrared spectrometer (FTIR) [66]. In the shaded region viusalized in Fig 3, no oxidation products, i.e., CO and $CO_2$, are detected via the applied gas phase diagnostics.

In the TGA profiles at $T > 600$ K significant differences are evident. In this temperature region, the release of CO and $CO_2$ is detected. The soot particles emitted at $SOI = 310$ °CA (OP i.) are the most reactive. At $T < 800$ K the conversion profile attains its maximum and exhibits a second comparatively flat peak at $T \sim 900$ K. Delaying $SOI$ by 30 °CA (OP ii.), the second peak at $\sim 900$ K, indicating a less-reactive fraction, rises, whereas the height of the first conversion peak at $T < 800$ K, caused by more-reactive particles, decreases. At further delay to $SOI = 250$ °CA (OP iii.), both conversion peaks are approximately equal. Soot particles emitted at the latest $SOI$, i.e., $SOI = 220$ °CA (OP iv.), reveal a unimodal conversion peak at $\sim 900$ K, indicating that the reactive fraction is formed to a very low amount. By reducing the equivalence ratio $\Phi$ and increasing the oxygen concentration in the mixture, the unimodal conversion curve is shifted to lower temperatures, indicating the formation of soot particles with an increasing reactivity against oxidation. Finally, Fig. 3 contains the conversion profile of soot from OP vi, indicating uniform highly non-reactive particles, which are oxidized at $T > 900$ K and in a narrow temperature range. In summary, the emitted soot contains varying fractions with different reactivity depending on the operating conditions.

The reactivity indices $RI$ of the OPs i. to vi. defined by Eq. (3) are listed in Table 2. According to Eq. (3), this normalized quantity requires a maximum and minimum reference particle system. Here, the maximum reactive system is represented by the soot particles emitted by the GDI engine with $SOI = 310$ °CA [32]. Graphite, the crystalline and therefore most non-reactive carbon configuration [44], serves as the second reference system. The gradual shift of the conversion of the reactive fractions to temperatures $T < 800$ K with varying $SOI$ as demonstrated in Fig. 3 is excellently represented by $RI$. It should be noted that $RI$ according to Eq. (3) represents contributions of all soot fractions contained in the sampled soot. The decrease of the reactivity index is connected with an increase of the soot volume fractions $f_V$ ranging from 1.2 ppb to 25 ppb for OP ii. to OP vi.

#### 3.1.2. Carbon nanostructure via HRTEM and EA

Table 3 containes the nanostructural properties of soot particles from OPs i. to vi. as evaluated from HRTEM images using the pattern recognition algorithm from ref. [23]. Here, $\overline{L_f}$ denotes the arithmetic mean of the frequency distribution $P(L_f)$ of the BSU size, while $L_{f,90}$ represents the ninth decile of the distribution and $L_{f,max}$ refers to the maximum detected BSU size. The quantities given in Table 3 calculated from HRTEM images include primary particles of different soot fractions if contained in the sampled soot.

The parameters of the BSU size distribution $P(L_f)$ increase with delayed fuel injection, i.e., from $SOI = 310$ °CA to 220 °CA. Delaying $SOI$ reduces the time for mixture formation inside the cylinder, thereby continuously increasing the existence of inhomogeneous, fuel-rich combustion zones. Within these zones particles with large, extended BSUs are formed, likely due to high soot precursor concentrations, cf. the discussion in Hagen et al. [67]. The largest graphene-like BSUs appear in soot particles from OP

**Table 1**
Investigated engine operating points at a constant engine speed of $n = 2000$ rpm and a break mean effective pressure of $P_m = 800$ kPa. The start of injection $SOI$, the equivalence ratio $\Phi$ and the rail pressure $P_r$ were varied.

| OP | $SOI$ / °CA BTDC | $\Phi$ / – | $P_r$ / kPa |
|---|---|---|---|
| 0.[a] | 310 | – | $10^4$ |
| i. | 310 | 1.0 | $10^4$ |
| ii. | 280 | 1.0 | $10^4$ |
| iii. | 250 | 1.0 | $10^4$ |
| iv. | 220 | 1.0 | $10^4$ |
| v. | 220 | 0.9 | $10^4$ |
| vi. | 280 and 70[b] | 1.1 | $5 \cdot 10^3$ |

[a] Transient cold start.
[b] Double fuel injection with 60 % at $SOI = 280$ °CA BTDC.

**Table 2**
Reactivity indices of the investigated GDI engine generated soot samples.

| OP | $RI$ / – |
|---|---|
| i. | 1.00 |
| ii. | 0.96 |
| iii. | 0.88 |
| iv. | 0.74 |
| v. | 0.84 |
| vi. | 0.61 |

**Table 3**
Carbon nanostructural quantities of GDI engine generated soot samples.

| OP | $\overline{L_f}$ / Å | $L_{f,90}$ / Å | $L_{f,max}$ / Å | C/H ratio / – |
|---|---|---|---|---|
| i. | $4.93 \pm 0.17$ | $7.03 \pm 0.41$ | $20.08 \pm 2.44$ | 1.23 |
| ii. | $5.14 \pm 0.08$ | $7.45 \pm 0.15$ | $24.24 \pm 2.44$ | 1.45 |
| iii. | $5.35 \pm 0.34$ | $7.95 \pm 0.71$ | $27.84 \pm 9.86$ | 2.13 |
| iv. | $5.68 \pm 0.67$ | $8.75 \pm 1.51$ | $34.18 \pm 6.42$ | 2.43 |
| v. | $5.34 \pm 0.03$ | $8.03 \pm 0.11$ | $29.42 \pm 3.87$ | –[a] |
| vi. | $5.76 \pm 0.15$ | $9.02 \pm 0.41$ | $41.38 \pm 5.39$ | –[a] |

[a] No elemental analysis possible due to insufficient amount of soot.

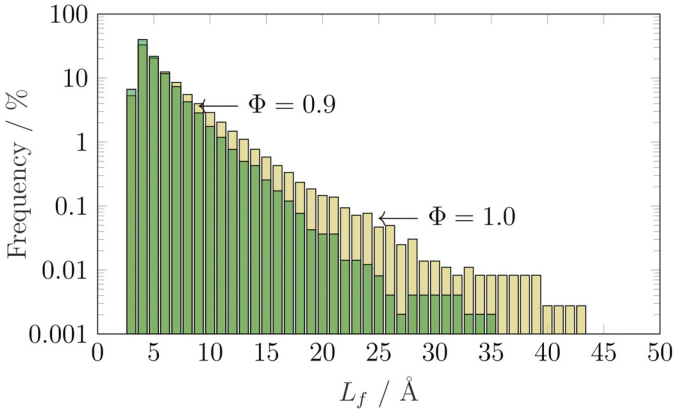


**Fig. 4.** Frequency distributions of the BSU size $P(L_f)$ for soot particles sampled during steady-state operation of $SOI = 220$ °CA at $\Phi = 1.0$ (OP iv.) and 0.9 (OP v.).

vi., where unfavorable mixture homogenization prevails due to the delayed second fuel injection in combination with the increased equivalence ratio and the reduced rail pressure. These findings are confirmed by the molar C/H ratios determined via elemental analysis. An increase of the BSU sizes connected with a broadening of $P(L_f)$, causes an increase in the molar C/H ratio, so that a delay of *SOI* increases not only $L_f$ but also the molar C/H ratio of the soot particles.

By reducing the equivalence ratio at $SOI = 220$ °CA (OP v.), the BSU size distribution $P(L_f)$ is shifted to shorter graphene-like structures, see Fig. 4. This can be explained by increased in-cylinder post-oxidation at lower equivalence ratio, causing a fragmentation of BSUs along with a size reduction according to Hagen et al. [68].

### 3.1.3. Carbon nanostructure and reactivity of different soot fractions

It should be noted that the TGA conversion profiles of soot particles from OPs iv. and v. exhibit one maximum, indicating the presence of predominantly one soot fraction with low reactivity. In contrast, the TGA conversion profiles of soot particles collected during OP ii. and OP iii. (and to a lower extent OP i.) exhibit two maxima, see Fig. 3. Soot aggregates from these operation points contain primary particles of different nanostructure as verified by HRTEM images of a single soot aggregate from OP ii. in Fig. 5.

Figure 6 provides the BSU size distributions of the two regions (ROIs) A. and B. from Fig. 5. It is obvious, that particles within ROI A. contain larger BSUs compared to ROI B., which corresponds with the visual impression in Fig. 5. The BSU size ranges up to 25 Å to 30 Å for the ROI A. and up to 15 Å to 20 Å for the carbon topology shown in ROI B. Connecting $\overline{L_f}$ with *RI* or the oxidation rates from dynamic TGA experiments [44], we can assume that the carbon topology shown in ROI B. corresponds to the low-temperature conversion peak at $T < 800$ K, while the carbon configuration of ROI A. is associated with the high-temperature peak at $T \sim 900$ K. This finding is supported by Hagen et al. [68], where it is demonstrated that each primary particle within an aggregate comprising a different nanostructure is subject to its own oxidation history. From that, possibly nanostructural inhomogeneities of soot aggregates and primary particles emitted at $SOI = 280$ °CA explain the distinct double peak in the TGA profile, see Fig. 3.

The most reactive particles predominantly contained in soot emitted at $SOI = 310$ °CA (OP i.) exhibit the shortest $L_f$. Short BSUs connected with a small C/H ratio are embedded within those reactive soot particles being oxidized at $\sim 800$ K. The increased reactivity may be traced back to an increased share of BSU edge site carbon atoms and C–H groups being preferentially accessed by oxidative species. Delaying *SOI* by 30 °CA in OP ii. and OP iii. leads to TPO profiles with two maxima. The characteristic size parameters of $P(L_f)$ including particles from both conversion peaks increase, which explains the reduced average (including both conversion peaks) soot reactivity indicated by the *RIs* in Table 2. The TPO profiles with two maxima arise from a reactive and a non-reactive fraction contained in these soot samples, as demonstrated for a soot aggregate from OP ii. in Fig. 5. Most likely, non-reactive soot particles are formed in fuel-rich zones with an increased soot precursor concentration, which may preferably bond to long BSUs [67]. In contrast, the reactive fraction emitted during OP ii. seems to result from homogeneous combustion zones, similar to OP i. Overall, the primary particles with different nanostructures result from inhomogeneous conditions during the combustion of the cylinder charge.

The largest BSUs are analyzed for soot particles emitted during OP vi. In turn, this explains the narrow and comparatively high temperature window for the oxidation of these particles.

**Table 4**
Count median diameter *CMD* and geometric standard deviation $\sigma_g$ of the primary particle size distributions $P(d_P)$ evaluated by HRTEM and TiRe-LII for the GDI engine generated soot particle ensembles.

| | HRTEM | | | TiRe-LII[a] |
|---|---|---|---|---|
| OP | *CMD* / nm | $\sigma_g$/– | $R^2$/– | *CMD* / nm |
| i. | 22.9 | 1.42 | 0.96 | 16.6 ± 5.8 |
| ii. | 22.0 | 1.35 | 0.97 | 16.8 ± 6.0 |
| iii. | 20.2 | 1.42 | 0.99 | 18.5 ± 7.5 |
| iv. | 21.4 | 1.36 | 0.98 | 17.4 ± 7.4 |
| v. | 21.4 | 1.35 | 0.99 | 16.7 ± 5.7 |
| vi. | 19.6 | 1.47 | 0.97 | 18.0 ± 6.2 |

[a] Values (±) were computed using $\sigma_g$ from HRTEM.

### 3.1.4. Primary particle size distributions

Figure 7 depicts the primary particle size distribution as evaluated from HRTEM images for OP iv. As described in Hagen et al. [44], the primary particle size distribution is fitted with a log-normal size distribution, with the count median diameter *CMD* and geometric standard deviation $\sigma_g$, equivalent to the first and second moments of the distribution.

Table 4 lists the *CMD*, $\sigma_g$, and quality of fits $R^2$ evaluated from HRTEM images for the particles collected during the investigated engine operating points and data obtained from TiRE-LII. The values correspond in good approximation to other engine generated soot samples as reported in e.g., [32,34,37,47]. The *CMDs* determined by TiRe-LII represent time-averaged values covering different particle ensembles examined during an OP and, therefore, exhibit a considerable span. The *CMD* and $\sigma_g$ and, therefore, $P(d_P)$ vary only marginally and non-systematically for the different OPs, while significant differences in soot reactivity were detected. This is in line with the findings reported in the references above. Similar to results presented in Kock et al. [14], Hagen et al. [44,52], the agreement between the particle size distributions derived via HRTEM and TiRe-LII is reasonable. Uncertainties in TiRe-LII may be attributed to a multitude of parameters in the numerical LII model affecting the computation of the particle size distributions, as discussed in more detail by Daun et al. [69] and Bauer et al. [16]. Besides the temperature-dependent particle parameters, such as density or specific heat capacity, especially the choice of the accommodation coefficient affects the evaluation of primary particle size distributions [16,69]. Furthermore, fluctuating local gas temperatures [70] or local fluence fluctuations, e.g., due to beam steering [71], also adversely affect the accuracy of the estimated size distributions.

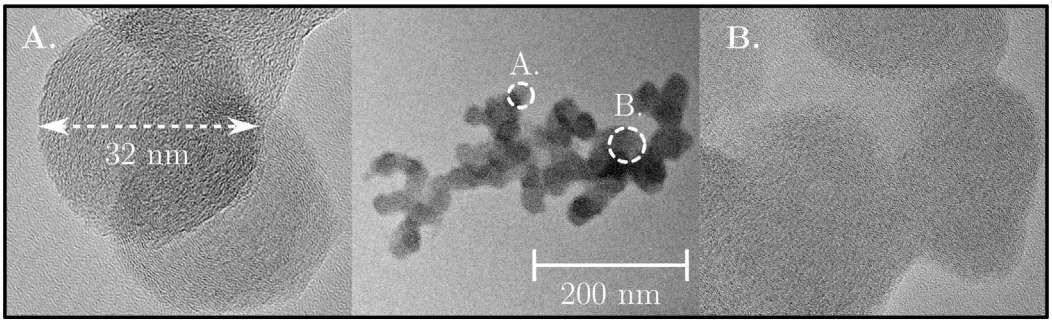


**Fig. 5.** HRTEM images of a soot aggregate sampled during steady-state operation of $SOI = 280$ °CA (OP ii.). The magnification of the two ROIs, A. and B., is the same.

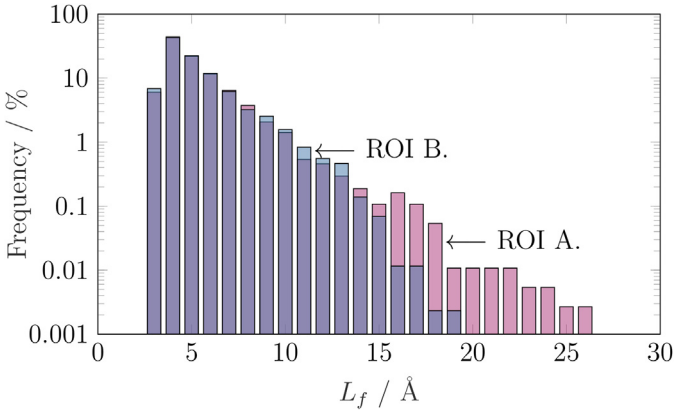


**Fig. 6.** BSU size distributions $P(L_f)$ for ROI A. and ROI B. indicated in Fig. 5.

### 3.2. On-line monitoring of carbon nanostructure and soot reactivity

The DP-2C-TiRe-LII enables the quantification of the ratio of refractive-index function for absorption for each single particle ensemble distributed in the detection volume at the time of the dual-pulse sequence [52]. Therefore, DP-2C-TiRe-LII can be applied to study nanostructural inhomogeneous aerosols under transient conditions.

First $E(m, \lambda_{UV})/E(m, \lambda_{NIR})$ of the particles formed under transient cold start conditions (OP 0.) were investigated applying DP-2C-TiRe-LII. The GDI engine had a surface temperature of 283 K at the start of the experiment. Under these conditions, fuel enrichment in gasoline engines ensures ignition [72]. The resulting fuel rich combustion implies an increased soot formation. Compared to port fuel injection (PFI), soot volume fractions in GDI engines are further increased due to the wetting of cold surfaces by impinging liquid fuel droplets [73].

Badshah et al. [73] showed that the mass of the particles emitted in the first thirty seconds after the cold start is three times larger than that during the second thirty second interval. In the third interval, the cumulative mass is reduced by half, while for $t > 90$ s a decrease of one order of magnitude can be observed. In [66] these findings were confirmed by measuring the particle number densities during cold start cycles.

This behavior explains the course of $E(m, \lambda_{UV})/E(m, \lambda_{NIR})$ versus time in Fig. 8, where the time-resolved ratios of the refractive-index function for absorption of soot particles emitted during the engine cold start are plotted in terms of a box-whisker plot. Initially, $E(m, \lambda_{UV})/E(m, \lambda_{NIR}) = 0.5 \ldots 1.0$ is observed. Within the first sixty to ninety seconds after initial ignition, the ratios increase

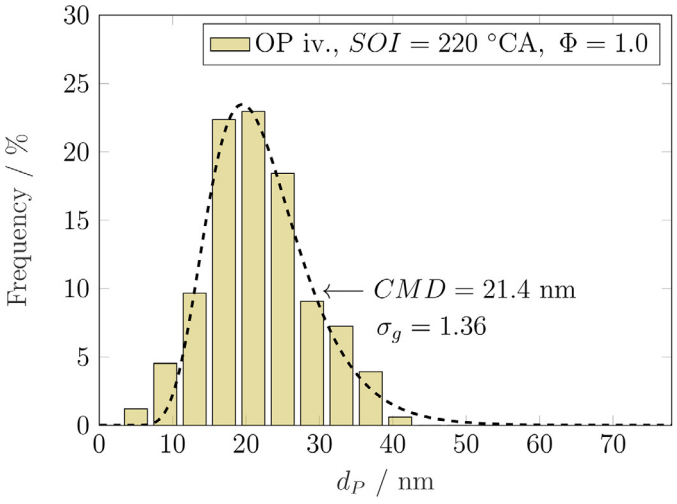


**Fig. 7.** Primary particle size distribution $P(d_P)$ including the fitted log-normal function of the soot particle ensemble emitted during OP iv.

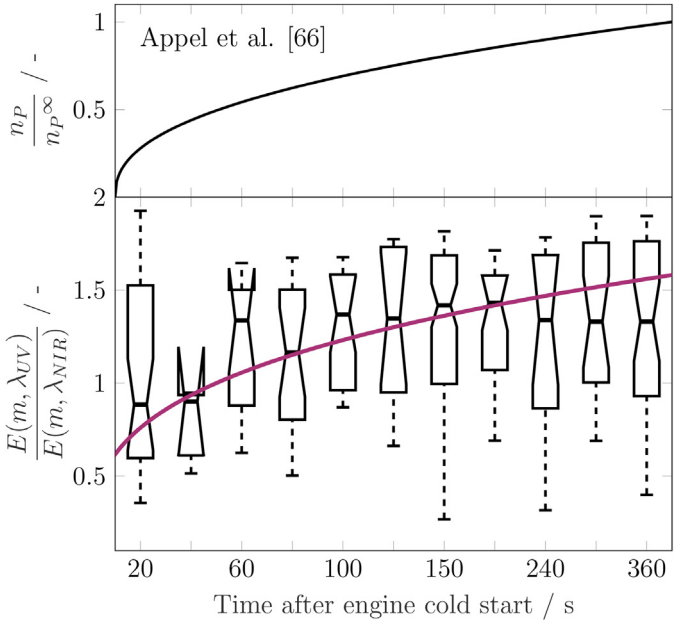


**Fig. 8.** Normalized, time-resolved cumulative particle number density after cold start of a GDI engine at $T = 283$ K according to Appel et al. [66] (upper plot). Box-whisker plot of the time-resolved evolution of the ratio of the refractive-index function for absorption $E(m, \lambda_{UV})/E(m, \lambda_{NIR})$ with $\lambda_{UV} = 355$ nm during the transient cold start cycle. The evolving mean value over time is displayed as solid red line (lower plot). In box-whisker plots the top and bottom of the boxes represent the first and third quantiles, respectively, of the distribution, while the center line indicates the medians, i.e., second quantiles. The whiskers specify the range of the measured values.

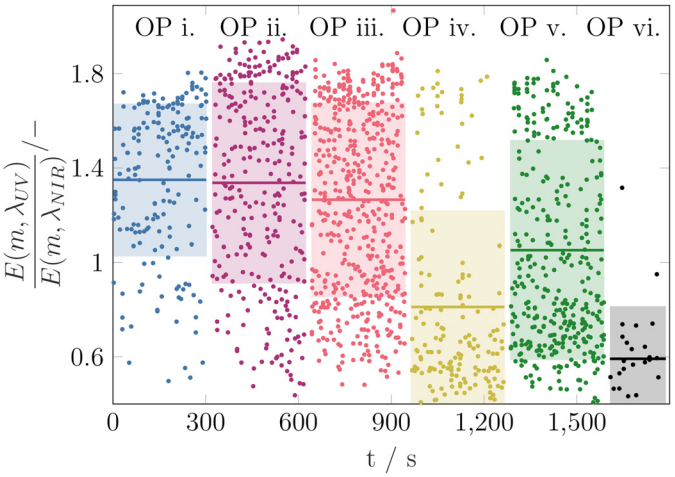


**Fig. 9.** Time-resolved single values of the ratios of the refractive-index function for absorption $E(m,\lambda_{UV})/E(m,\lambda_{NIR})$ with $\lambda_{UV} = 355$ nm. The mean values obtained from the single coincidences for the engine operating points i. to vi. are shown as a line, while the shaded areas classify the standard deviation.

rapidly and then approach a value of $E(m,\lambda_{UV})/E(m,\lambda_{NIR}) \approx 1.5$. Within the same period after cold start, the temperature of the cylinder walls increases and combustion inside the cylinder becomes more homogeneous, resulting in a decrease of $f_V$ [73]. This decrease of $f_V$ is connected with a decrease of the soot precursor concentrations as well as a decrease of the mean BSU size within primary particles [67]. The band gap energy for an electronic $\pi \rightarrow \pi^*$ transition in conjugated $\pi$ systems, i.e., BSUs, becomes increasingly broader with decreasing size of the BSUs. Thereby the wavelength of light absorbed becomes correspondingly shorter, causing $E(m,\lambda_{UV})/E(m,\lambda_{NIR})$ to increase [52,74,75]. The continuously increasing $E(m,\lambda_{UV})/E(m,\lambda_{NIR})$ indicates a decrease of the size of the BSUs with increasing operating time of the engine during OP 0. Taking into account the correlations between the size of the BSUs and reactivity index of soot introduced in the following section, the reactivity of soot particles emitted during the engine cold start increases gradually from $RI \approx 0.6$ to $RI \approx 1.0$.

Clustering the values over a time interval of $\Delta t = 20$ s is required since the single samples measured with DP-2C-TiRe-LII scatter considerably. This may be due to the inhomogeneous fuel droplet size distribution and the resulting inhomogeneous combustion regimes [76], in which particles of strongly different nanostructural topology probably are formed [32].

The time-resolved evolution of $E(m,\lambda_{UV})/E(m,\lambda_{NIR})$ for OPs i. to vi. is depicted in Fig. 9. The ratio $E(m,\lambda_{UV})/E(m,\lambda_{NIR})$ approaches $\approx 1.5$ at the end of OP 0., which corresponds roughly to the mean value of OP i. The mean values of $E(m,\lambda_{UV})/E(m,\lambda_{NIR})$ determined for each operating point are within the range of values given by Yon et al. [77] and Bejaoui et al. [78], while following the inverse volume fraction as proposed in Hagen et al. [67].

To reconstruct reactivity indices as well as the carbon nanostructure, correlations between $E(m,\lambda_{UV})/E(m,\lambda_{NIR})$, $RI$ and $L_f$ are needed. In [44] we derived linear relationships between these quantities using carefully selected particle systems and $\lambda_{UV} =$ 266 nm. Figure 10 shows similar correlations for the engine generated particle ensembles investigated in this study using $\lambda_{UV} =$ 355 nm. Again, we find linear correlations that seem to allow an in situ estimation of $RI$ and $L_f$ via non-intrusive measurement of $E(m,\lambda_{UV})/E(m,\lambda_{NIR})$. For this case we preferred $L_{f,90}$ as dependent variable due to the larger slope of the linear correlation and, hence, the larger sensitivity of $E(m,\lambda_{UV})/E(m,\lambda_{NIR})$ against $L_{f,90}$ [44]. Taking into account these relationships, inhomogeneous fuel-rich combustion zones resulting from delayed fuel injection favor the formation of non-reactive soot particles.

The broad distributions of BSU sizes of primary particles formed in the GDI engine, compare Section 3.1.2, is not only reflected in the broad temperature window for the oxidation with oxygen, see Fig. 3, but also in the scattered values of $E(m,\lambda_{UV})/E(m,\lambda_{NIR})$, see Figs. 8 and 9. From that, it is reasonable that the wide scatter of the measured data is due to the nanostructure of the primary particles, rather than to measurement errors. Qualitatively, this is substantiated by fitting $E(m,\lambda_{UV})/E(m,\lambda_{NIR})$, BSU sizes and RI data to the correlations suggested in refs. [44,52]. The quantita-

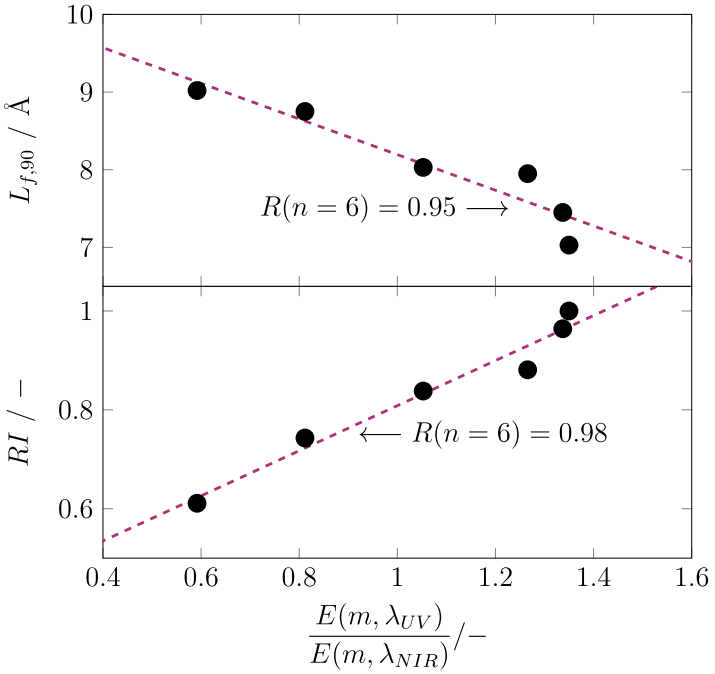


**Fig. 10.** Mean ratios of the refractive-index function for absorption $E(m,\lambda_{UV})/E(m,\lambda_{NIR})$ with $\lambda_{UV} = 355$ nm as function of the ninth decile of $P(L_f)$ (top) and $RI$ (bottom). The dashed lines represent linear regressions with Pearson's correlation coefficients $R$.

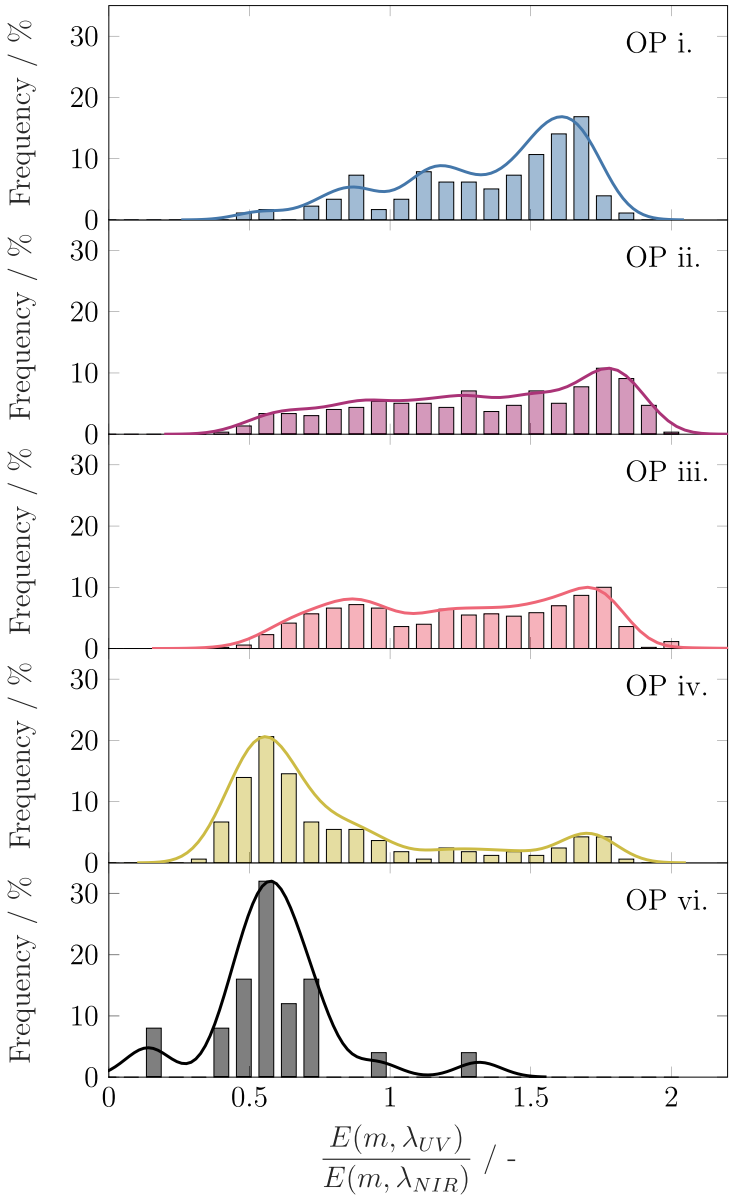


**Fig. 11.** Probability density distributions of the ratio of refractive-index function for absorption $E(m,\lambda_{UV})/E(m,\lambda_{NIR})$ with $\lambda_{UV} = 355$ nm and the associated kernel density estimates according to Parzen [81].

tive substantiation can be provided by the Friedman test [79,80], which is used to estimate the statistical significance of the differences between the masured values from the different OPs. The Friedman test presumes no normal distributions of the sample data and is a non-parametric method [79,80]. The larger the differences between the rank sums of the individual samples, the lower the $p$-value as a measure of statistical significance. For the measured data set, a $p$-value of 0.037 is computed, which is smaller than the typically specified significance level of 0.050. Therefore, the measured differences can be considered statistically significant.

Note that each dot in Fig. 9 indicating signal coincidence characterizes the ratio of the refractive-index function for absorption of a particular particle group. Therefore, the colored shaded standard deviations represent the width of the statistically distributed single values of $E(m,\lambda_{UV})/E(m,\lambda_{NIR})$. The same applies to the particle ensembles emitted during cold start conditions. Temporal nanostructural fluctuations may therefore be resolved and do not disappear by averaging over the particle ensemble, which is a major advantage of DP-2C-TiRe-LII.

The transformation of the time series of $E(m,\lambda_{UV})/E(m,\lambda_{NIR})$ into probability density distributions is presented in Fig. 11. As discussed above, the probability densities correspond to the BSU size distributions, i.e., they shift to smaller ratios with increasing $\overline{L_f}$. Accordingly, the TPO conversion profiles during oxidation are mirrored distributions of $E(m,\lambda_{UV})/\ E(m,\lambda_{NIR})$. The double peak conversion profiles reflected by both nanostructural topologies verified via HRTEM, can be recognized from the $E(m,\lambda_{UV})/E(m,\lambda_{NIR})$ distributions. While large BSUs exhibit a value of $E(m,\lambda_{UV})/E(m,\lambda_{NIR})$ larger than 1.0, short BSUs absorb at near-infrared only poorly, yielding $E(m,\lambda_{UV})/E(m,\lambda_{NIR}) \approx 1.5$. The narrow distribution shifted to small ratios for particles from OP vi, supports the high-temperature window for particle oxidation.

By measuring the particle temperature after laser pulse heating via 2C detection optics, the values of $E(m,\lambda_{UV})/E(m,\lambda_{NIR})$ can even be transformed into the absolute distributions of $E(m,\lambda_{UV})$ and $E(m,\lambda_{NIR})$. Details reagarding this approach are reported in Hagen et al. [52], Török et al. [57]. By transforming, $E(m,\lambda_{UV})$ remains largely unchanged, while $E(m,\lambda_{NIR})$ varies between 0.1 and 0.5 depending on the nanostructural particle topology. These

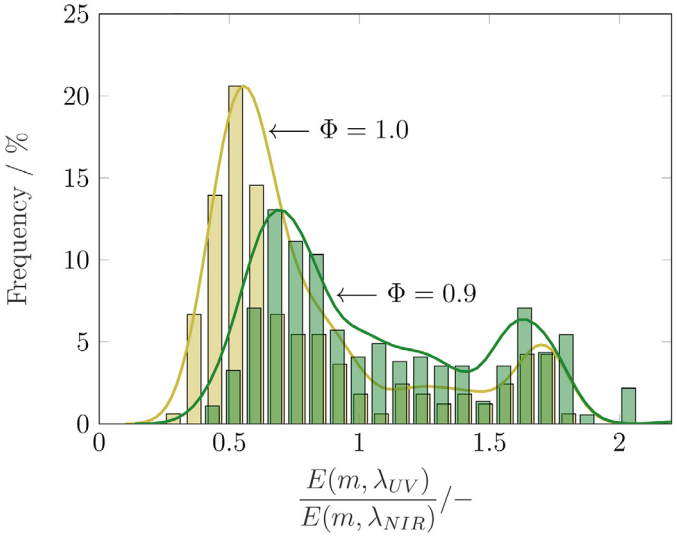


**Fig. 12.** Probability density distributions of the ratio of refractive-index function for absorption $E(m,\lambda_{UV})/E(m,\lambda_{NIR})$ with $\lambda_{UV} = 355$ nm for $SOI = 220$ °CA with $\Phi = 1.0$, OP iv. and 0.9, OP v., including the associated kernel density estimates according to Parzen [81].

values are in good agreement with those reported in refs. [55,57,77,82–85]. Liu et al. [86] recommend $E(m,\lambda)$ values of 0.35 to 0.45 in the visible and near-infrared, respectively. This recommendation refers to mature black carbon, meaning high degree of graphitization, high C/H ratio and high elemental carbon content. Values of 0.5 for $E(m,\lambda_{NIR})$ fit into that scheme whereas values of 0.1 lie beyond this recommendation. As illustrated by Fig. 11, the probability density distributions of $E(m,\lambda_{UV})/E(m,\lambda_{NIR})$ exhibit multimodal shapes indicating primary soot particles of different degree of graphitization. This is reflected by the size distributions of graphene layers as illustrated in Figs. 5 and 6 for an aggregate collected in OP ii. Due to the non-homogeneous combustion conditions in the GDI engine, soot primary particles with different degrees of graphitization, i.e., different size of graphene layers, are formed, which absorb at different wavelengths. Values of $E(m,\lambda_{NIR})$ smaller than 0.35 can be traced back to these *non-matured* primary particles.

Partial soot oxidation is associated with BSU fragmentation [68]. Therefore, the mean value of $E(m,\lambda_{UV})/E(m,\lambda_{NIR})$ increases for the particles formed under the oxygen-rich combustion conditions of OP v. This can be derived from Fig. 9 comparing OP iv. and v. The corresponding time series transformed into a probability density distributions are given in Fig. 12 and confirm the fragmentation of BSUs as previously demonstrated via nanostructure analysis, see Section 3.1.2. The large BSUs formed during stoichiometric combustion exhibiting $E(m,\lambda_{UV})/E(m,\lambda_{NIR}) \approx 0.5$ are apparently fragmented into shorter structures during (and likely after) soot formation. Their absorption in the near-infrared is reduced, accounting for the considerable shift of $E(m,\lambda_{UV})/E(m,\lambda_{NIR})$ towards larger values, see Fig. 12.

As discussed in detail in ref. [52], the temporal resolution of the DP-2C-TiRe-LII depends exclusively on the modulated fluence of the near-infrared laser pulses, i.e., the modulation frequency, and the repetition rate of the two pulse lasers. Although the latter cannot be varied in our experimental setup, a detection rate of $\sim 1.0$ Hz is achieved in the presented experiments. A possibility to increase the detection rate could be the limitation of the fluence of the near-infrared laser to a range expected for the prevailing particle system. In combination with increasing the repetition rates of the lasers, detection rates of some kHz possibly can be achieved.

## 4. Summary and concluding remarks

While a rapid and non-intrusive diagnostic of the primary particle size distribution $P(d_P)$ of engine generated soot has already been demonstrated [87,88], the analysis of the statistical moments of the BSU size distribution $P(L_f)$, and via this the carbon nanostructure, requires a non-trivial intrusive particle sampling as well as time-consuming electron microscopic experiments combined with pattern recognition algorithm [44]. The same applies to soot reactivity against oxidation, which is a nano-structure-associated particle property of crucial interest for exhaust gas aftertreatment methods. To enable a simultaneous in situ quantification of the nanostructural particle topology and reactivity index, DP-2C-TiRe-LII was introduced in Hagen et al. [52]. On the one hand, this approach provides $P(d_P)$ by a multidimensional nonlinear fit of the calculated size distributions to the measured TiRe-LII signal decays. On the other hand, nanostructure diagnostics based on the absorption of near-infrared laser light is determined by $P(L_f)$. Applying quantitative correlations between carbon nanostructure and soot reactivity, their non-intrusive on-line monitoring become accessible through recording of readily available ratios of refractive-index functions for absorption at two wavelengths $E(m,\lambda_{UV})/E(m,\lambda_{NIR})$ [44]. The work presented here provides the proof-of-principle of this approach by employing DP-2C-TiRe-LII in the exhaust gas of a GDI engine running under both steady-state and transient operating conditions.

First, $E(m,\lambda_{UV})/E(m,\lambda_{NIR})$ of particles formed under transient cold start conditions were investigated. The increasing temperatures of the cylinder walls within the first ninety seconds after the cold start and the consequently more homogeneous combustion conditions, cause continuously increasing $E(m,\lambda_{UV})/E(m,\lambda_{NIR})$ values indicating a decrease of the first moment of $P(L_f)$ with increasing operating time. Applying the correlation proposed in this work, the reactivity of the soot particles emitted during cold start of the GDI engine gradually increases from $RI \approx 0.6$ to 1.0. These findings are particularly important when dealing with fouling of exhaust gas-carrying components, as critically discussed in e.g., [66] and which is subject of current research.

Second, seven selected engine operating points introduced in Koch et al. [32,36] are investigated using DP-2C-TiRe-LII. In addition, intrusive particle sampling during the steady-state periods enables a comprehensive analytical ex situ quantification of carbon nanostructure and reactivity for validation of the DP-2C-TiRe-LII results. The applied analytical toolbox comprises HRTEM in combination with pattern recognition methods, EA, and TGA. Excellent agreement was found between the particle properties derived via ex situ and in situ diagnostics. Moreover, the transformation of the time series of $E(m,\lambda_{UV})/E(m,\lambda_{NIR})$ into probability density distributions represent the BSU size distributions of the investigated soot particles. Also, the conversion profiles during TGA oxidation experiments are reflected in the distributions of $E(m,\lambda_{UV})/E(m,\lambda_{NIR})$.

The findings obtained are not exclusively valid for soot reactivity, but can be transferred to any nanostructure-associated particle property, e.g., electrical conductivity [89], biological reactivity [90] *et cetera*. Once quantitative correlations between a desired nanostructure-associated particle property and the nanostructure are derived, the application of DP-2C-TiRe-LII enables on-line monitoring of this quantity in applications from practice.

## Declaration of Competing Interest

The authors declare that they have no known competing financial interests or personal relationships that could have appeared to influence the work reported in this paper.

## Acknowledgments

The authors are very grateful to the German Research Foundation (DFG) for financial support within the research projects TR470/7-1/2, SU249/6-1/2, KO4830/2-1/2 and for funding measuring equipment within the HBFG program INST 121384/178-1 FUGG. The authors gratefully acknowledge the assistance of Dr. Heike Störmer from the Laboratory of Electron Microscopy at Karlsruhe Institute of Technology (KIT) in preparing electron microscopy images. Nicole Klaassen from the Institute for Inorganic Chemistry at KIT is kindly acknowledged for carrying out the elemental analyses. Lastly, the support of Lucas Büttner conducting the engine experiments is thankfully acknowledged.

## Appendix A. List of frequently used acronyms

| | | | |
|---|---|---|---|
| APM | aerosol particle mass analyzer | BSU | basic structural unit |
| BTDC | before top dead center | CA | crank angle |
| CMD | count median diameter | CVS | constant volume sampler |
| D | diesel | DP | dual-pulse |
| DR | dilution ratio | EA | elemental analysis |
| FTIR | Fourier-transform infrared | FWHM | full width at half maximum |
| GDI | gasoline direct injection | GPF | gasoline particulate filter |
| HRTEM | high-resolution transmission electron microscopy | ICE | internal combustion engine |
| IR | infrared | LII | laser-induced incandescence |
| NIR | near infrared | OP | operating point |
| PA | photoacoustic | PF | particulate filter |
| QMS | quadrupole mass spectrometer | RDG-FA | Rayleigh–Debye–Gans theory for fractal aggregates |
| RI | reactivity index | ROI | region of interest |
| RON | research octane number | RS | Raman spectroscopy |
| SOI | start of injection | TCD | thermoconductivity |
| TDMA | tandem differential mobility analyzer | TGA | thermogravimetric analysis |
| TiRe | time-resolved | TPO | temperature-programmed oxidation |
| TWC | three-way catalytic converter | UV | ultraviolet |
| VOC | volatile organic compounds | XRD | X-ray diffraction |
| 2C | two-color | | |

## References

[1] K. Donaldson, X. Li, W. MacNee, Ultrafine (nanometre) particle mediated lung injury, J. Aerosol. Sci. 29 (1998) 553–560, doi:10.1016/S0021-8502(97)00464-3.
[2] I.M. Kennedy, The health effects of combustion-generated aerosols, Proc. Combust. Inst. 31 (2007) 2757–2770, doi:10.1016/j.proci.2006.08.116.
[3] P. Cariñanos, C. Galán, P. Alcázar, E. Dominguez, Meteorological phenomena affecting the presence of solid particles suspended in the air during winter, Int. J. Biometeorol. 44 (2000) 6–10, doi:10.1007/s004840050132.
[4] E.J. Highwood, R.P. Kinnersley, When smoke gets in our eyes: the multiple impacts of atmospheric black carbon on climate, air quality and health, Environ. Int. 32 (2006) 560–566, doi:10.1016/j.envint.2005.12.003.
[5] V. Ramanathan, G. Carmichael, Global and regional climate changes due to black carbon, Nat. Geosci. 1 (2008) 221–227, doi:10.1038/ngeo156.
[6] M.O. Andreae, P.J. Crutzen, Atmospheric aerosols: biogeochemical sources and role in atmospheric chemistry, Science 276 (1997) 1052–1058.
[7] T.C. Bond, S.J. Doherty, D.W. Fahey, P.M. Forster, T. Berntsen, B.J. DeAngelo, M.G. Flanner, S. Ghan, B. Kärcher, D. Koch, S. Kinne, Y. Kondo, P.K. Quinn, M.C. Sarofim, M.G. Schultz, M. Schulz, C. Venkataraman, H. Zhang, S. Zhang, N. Bellouin, S.K. Guttikunda, P.K. Hopke, M.Z. Jacobson, J.W. Kaiser, Z. Klimont, U. Lohmann, J.P. Schwarz, D. Shindell, T. Storelvmo, S.G. Warren, C.S. Zender, Bounding the role of black carbon in the climate system: a scientific assessment, J. Geophys. Res. Atmos. 118 (2013) 5380–5552.
[8] D.B. Kittelson, Engines and nanoparticles: a review, J. Aerosol Sci. 29 (1998) 575–588, doi:10.1016/S0021-8502(97)10037-4.
[9] I. Glassman, Soot formation in combustion processes, Proc. Combust. Inst. 22 (1989) 295–311, doi:10.1016/S0082-0784(89)80036-0.
[10] H. Bockhorn, Soot Formation in Combustion: Mechanisms and Models, Springer-Verlag Berlin Heidelberg, 1994.
[11] J. Appel, H. Bockhorn, M. Frenklach, Kinetic modeling of soot formation with detailed chemistry and physics: laminar premixed flames of $C_2$hydrocarbons, Combust. Flame 121 (2000) 122–136, doi:10.1016/S0010-2180(99)00135-2.
[12] H. Bockhorn, F. Fetting, A. Heddrich, G. Wannemacher, Untersuchung der bildung und des wachstums von rußteilchen in vorgemischten kohlenwasserstoff – sauerstoff unterdruckflammen, Ber. Bunsenges. Phys. Chem. 91 (1987) 819–825.
[13] A. Boiarciuc, F. Foucher, C. Mounaïm-Rousselle, Soot volume fractions and primary particle size estimate by means of the simultaneous two-color-time-resolved and 2D laser-induced incandescence, Appl. Phys. B 83 (2006) 413, doi:10.1007/s00340-006-2236-8.
[14] B.F. Kock, B. Tribalet, C. Schulz, P. Roth, Two-color time-resolved LII applied to soot particle sizing in the cylinder of a diesel engine, Combust. Flame 147 (2006) 79–92, doi:10.1016/j.combustflame.2006.07.009.
[15] H. Michelsen, Probing soot formation, chemical and physical evolution, and oxidation: a review of in situ diagnostic techniques and needs, Proc. Combust. Inst. 36 (2017) 717–735, doi:10.1016/j.proci.2016.08.027.
[16] F.J. Bauer, K.J. Daun, F.J.T. Huber, S. Will, Can soot primary particle size distributions be determined using laser-induced incandescence? Appl. Phys. B 125 (2019) 109, doi:10.1007/s00340-019-7219-7.
[17] C.M. Sorensen, G.D. Feke, The morphology of macroscopic soot, Aerosol Sci. Technol. 25 (1996) 328–337, doi:10.1080/02786829608965399.
[18] M. Altenhoff, S. Aßmann, J.F.A. Perlitz, F.J.T. Huber, S. Will, Soot aggregate sizing in an extended premixed flame by high-resolution two-dimensional multi-angle light scattering (2D-MALS), Appl. Phys. B 125 (2019) 176, doi:10.1007/s00340-019-7282-0.
[19] R.L. Vander Wal, A.J. Tomasek, M.I. Pamphlet, C.D. Taylor, W.K. Thompson, Analysis of HRTEM images for carbon nanostructure quantification, J. Nanopart. Res. 6 (2004) 555–568, doi:10.1007/s11051-004-3724-6.
[20] R.L. Vander Wal, A.J. Tomasek, K. Street, D.R. Hull, W.K. Thompson, Carbon nanostructure examined by lattice fringe analysis of high-resolution transmission electron microscopy images, Appl. Spectrosc. 58 (2004) 230–237. http://www.osapublishing.org/as/abstract.cfm?URI=as-58-2-230
[21] D. Su, R. Jentoft, J.-O. Müller, D. Rothe, E. Jacob, C. Simpson, Ž. Tomović, K. Müllen, A. Messerer, U. Pöschl, R. Niessner, R. Schlögl, Microstructure and oxidation behaviour of Euro IV diesel engine soot: a comparative study with synthetic model soot substances, Catal. 90 (2004) 127–132, doi:10.1016/j.cattod.2004.04.017.
[22] S. Pfau, A. La Rocca, E. Haffner-Staton, G. Rance, M. Fay, R. Brough, S. Malizia, Comparative nanostructure analysis of gasoline turbocharged direct injection and diesel soot-in-oil with carbon black, Carbon 139 (2018) 342–352, doi:10.1016/j.carbon.2018.06.050.
[23] F. Hagen, F. Hardock, S. Koch, N. Sebbar, H. Bockhorn, A. Loukou, H. Kubach, R. Suntz, D. Trimis, T. Koch, Why soot is not alike soot: amolecular/nanostructural approach to low temperature soot oxidation, Flow, Turbul. Combust. 106 (2021) 295–329, doi:10.1007/s10494-020-00205-2.
[24] D. Kayes, S. Hochgreb, Mechanisms of particulate matter formation in spark-ignition engines. 1. Effect of engine operating conditions, Environ. Sci. Technol. 33 (1999) 3957–3967, doi:10.1021/es9810991.
[25] S.J. Harris, M. Maricq, Signature size distributions for diesel and gasoline engine exhaust particulate matter, J. Aerosol Sci. 32 (2001) 749–764, doi:10.1016/S0021-8502(00)00111-7.
[26] G. Saliba, R. Saleh, Y. Zhao, A.A. Presto, A.T. Lambe, B. Frodin, S. Sardar, H. Maldonado, C. Maddox, A.A. May, G.T. Drozd, A.H. Goldstein, L.M. Russell, F. Hagen, A.L. Robinson, Comparison of gasoline direct-injection (GDI) and port fuel injection (PFI) vehicle emissions: emission certification standards, cold-start, secondary organic aerosol formation potential, and potential climate impacts, Environ. Sci. Technol. 51 (2017) 6542–6552, doi:10.1021/acs.est.6b06509.
[27] M.M. Maricq, Engine, aftertreatment, fuel quality and non-tailpipe achievements to lower gasoline vehicle PM emissions: literature review and future prospects, Sci. Total Environ. 866 (2023) 161225, doi:10.1016/j.scitotenv.2022.161225.
[28] A. Konstandopoulos, E. Skaperdas, M. Masoudi, Microstructural properties of soot deposits in diesel particulate traps, SAE Tech.2002-01-1015(2002) 1–11.
[29] O.I. Awad, X. Ma, M. Kamil, O.M. Ali, Z. Zhang, S. Shuai, Particulate emissions from gasoline direct injection engines: a review of how current emission regulations are being met by automobile manufacturers, Sci. Total Environ. 718 (2020) 137302, doi:10.1016/j.scitotenv.2020.137302.
[30] A. Joshi, T.V. Johnson, Gasoline particulate filters - a review, Emission Control Sci. Technol. 4 (2018) 219–239, doi:10.1007/s40825-018-0101-y.
[31] C. McCaffery, H. Zhu, C. Li, T.D. Durbin, K.C. Johnson, H. Jung, R. Brezny, M. Geller, G. Karavalakis, On-road gaseous and particulate emissions from GDI vehicles with and without gasoline particulate filters (GPFs) using portable emissions measurement systems (PEMS), Sci. Total Environ. 710 (2020) 136366, doi:10.1016/j.scitotenv.2019.136366.
[32] S. Koch, F.P. Hagen, L. Büttner, J. Hartmann, A. Velji, H. Kubach, T. Koch, H. Bockhorn, D. Trimis, R. Suntz, Influence of global operating parameters on the reactivity of soot particles from direct injection gasoline engines, Emission Control Sci. Technol. 8 (2022) 9–35.
[33] K. Al-Qurashi, A.L. Boehman, Impact of exhaust gas recirculation (EGR) on the oxidative reactivity of diesel engine soot, Combust. Flame 155 (2008) 675–695, doi:10.1016/j.combustflame.2008.06.002.
[34] U. Leidenberger, W. Mühlbauer, S. Lorenz, S. Lehmann, D. Brüggemann, Experimental studies on the influence of diesel engine operating parameters on properties of emitted soot particles, Combust. Sci. Technol. 184 (2012) 1–15, doi:10.1080/00102202.2011.611551.

[35] S. Choi, H. Seong, Oxidation characteristics of gasoline direct-injection (GDI) engine soot: catalytic effects of ash and modified kinetic correlation, Combust. Flame 162 (2015) 2371–2389, doi:10.1016/j.combustflame.2015.02.004.

[36] S. Koch, H. Kubach, A. Velji, T. Koch, F.P. Hagen, H. Bockhorn, A. Loukou, D. Trimis, R. Suntz, Impact of the injection strategy on soot reactivity and particle properties of a GDI engine, SAE Tech. 2020-01-0392 (2020) 1–15.

[37] A. Zygogianni, M. Syrigou, A.G. Konstandopoulos, M. Kostoglou, Oxidative reactivity of particulate samples from different diesel combustion systems and its relation to structural and spectral characteristics of soot, Emission Control Sci. Technol. 5 (2019) 99–123, doi:10.1007/s40825-019-00118-1.

[38] X. Liang, B. Zhao, K. Wang, X. Lv, Y. Wang, J. Liu, Y. Wang, Impact of multi-injection strategies on morphology, nanostructure and oxidation reactivity of diesel soot particles, Combust. Flame 237 (2022) 111854, doi:10.1016/j.combustflame.2021.111854.

[39] X. Zhang, C. Song, G. Lyu, Y. Li, Y. Qiao, Z. Li, Physicochemical analysis of the exhaust soot from a gasoline direct injection (GDI) engine and the carbon black, Fuel 322 (2022) 124262, doi:10.1016/j.fuel.2022.124262.

[40] C. Russo, A. Ciajolo, S. Cimino, V. La Matta, A. La Rocca, B. Apicella, Reactivity of soot emitted from different hydrocarbon fuels: effect of nanostructure on oxidation kinetics, Fuel Process. Technol. 236 (2022) 107401, doi:10.1016/j.fuproc.2022.107401.

[41] M.N. Ess, H. Bladt, W. Mühlbauer, S.I. Seher, C. Zöllner, S. Lorenz, D. Brüggemann, U. Nieken, N.P. Ivleva, R. Niessner, Reactivity and structure of soot generated at varying biofuel content and engine operating parameters, Combust. Flame 163 (2016) 157–169. https://www.sciencedirect.com/science/article/pii/S0010218015003193

[42] M. Knauer, M.E. Schuster, D. Su, R. Schlögl, R. Niessner, N.P. Ivleva, Soot structure and reactivity analysis by Raman microspectroscopy, temperature-programmed oxidation, and high-resolution transmission electron microscopy, J. Phys. Chem. A 113 (2009) 13871–13880, doi:10.1021/jp905639d.

[43] J. Schmid, B. Grob, R. Niessner, N.P. Ivleva, Multiwavelength Raman microspectroscopy for rapid prediction of soot oxidation reactivity, Anal. Chem. 83 (2011) 1173–1179, doi:10.1021/ac102939w.

[44] F.P. Hagen, D. Kretzler, T. Häber, H. Bockhorn, R. Suntz, D. Trimis, Carbon nanostructure and reactivity of soot particles from non-intrusive methods based on UV-VIS spectroscopy and time-resolved laser-induced incandescence, Carbon 182 (2021) 634–654, doi:10.1016/j.carbon.2021.06.006.

[45] R.L. Vander Wal, A.J. Tomasek, Soot oxidation: dependence upon initial nanostructure, Combust. Flame 134 (2003) 1–9, doi:10.1016/S0010-2180(03)00084-1.

[46] A. Rinkenburger, T. Toriyama, K. Yasuda, R. Niessner, Catalytic effect of potassium compounds in soot oxidation, ChemCatChem 9 (2017) 3513–3525.

[47] W. Mühlbauer, C. Zöllner, S. Lehmann, S. Lorenz, D. Brüggemann, Correlations between physicochemical properties of emitted diesel particulate matter and its reactivity, Combust. Flame 167 (2016) 39–51, doi:10.1016/j.combustflame.2016.02.029.

[48] S. Bensaid, N. Russo, D. Fino, $CeO_2$ catalysts with fibrous morphology for soot oxidation: the importance of the soot-catalyst contact conditions, Catal. Today 216 (2013) 57–63, doi:10.1016/j.cattod.2013.05.006.

[49] K.J. Higgins, H. Jung, D.B. Kittelson, J.T. Roberts, M.R. Zachariah, Size-selected nanoparticle chemistry: kinetics of soot oxidation, J. Phys. Chem. A 106 (2002) 96–103, doi:10.1021/jp004466f.

[50] X. Ma, C.D. Zangmeister, M.R. Zachariah, Soot oxidation kinetics: a comparison study of two tandem ion-mobility methods, J. Phys. Chem. C 117 (2013) 10723–10729, doi:10.1021/jp400477v.

[51] A. Rinkenburger, R. Niessner, C. Haisch, On-line determination of soot oxidation reactivity, J. Aerosol Sci. 132 (2019) 12–21, doi:10.1016/j.jaerosci.2019.03.002.

[52] F.P. Hagen, R. Suntz, H. Bockhorn, D. Trimis, Dual-pulse laser-induced incandescence to quantify carbon nanostructure and related soot particle properties in transient flows – concept and exploratory study, Combust. Flame 243 (2022) 112020, doi:10.1016/j.combustflame.2022.112020.

[53] P. Minutolo, G. Gambi, A. D'Alessio, The optical band gap model in the interpretation of the UV-visible absorption spectra of rich premixed flames, Proc. Combust. Inst. 26 (1996) 951–957, doi:10.1016/S0082-0784(96)80307-9.

[54] C. Jäger, T. Henning, R. Schlögl, O. Spillecke, Spectral properties of carbon black, J. Non-Cryst. Solids 258 (1999) 161–179, doi:10.1016/S0022-3093(99)00436-6.

[55] T. Williams, C. Shaddix, K. Jensen, J. Suo-Anttila, Measurement of the dimensionless extinction coefficient of soot within laminar diffusion flames, Int. J. Heat Mass Transf. 50 (2007) 1616–1630, doi:10.1016/j.ijheatmasstransfer.2006.08.024.

[56] S. Török, M. Mannazhi, S. Bergqvist, K.C. Le, P.-E. Bengtsson, Influence of rapid laser heating on differently matured soot with double-pulse laser-induced incandescence, Aerosol Sci. Technol. 56 (2022) 488–501, doi:10.1080/02786826.2022.2046689.

[57] S. Török, M. Mannazhi, P.-E. Bengtsson, Laser-induced incandescence (2λ and 2C) for estimating absorption efficiency of differently matured soot, Appl. Phys. B 127 (2021) 96, doi:10.1007/s00340-021-07638-1.

[58] C. Schulz, B.F. Kock, M. Hofmann, H. Michelsen, S. Will, B. Bougie, R. Suntz, G. Smallwood, Laser-induced incandescence: recent trends and current questions, Appl. Phys. B 83 (2006) 333, doi:10.1007/s00340-006-2260-8.

[59] H. Michelsen, C. Schulz, G. Smallwood, S. Will, Laser-induced incandescence: particulate diagnostics for combustion, atmospheric, and industrial applications, Prog. Energy Combust. Sci. 51 (2015) 2–48, doi:10.1016/j.pecs.2015.07.001.

[60] T. Lehre, B. Jungfleisch, R. Suntz, H. Bockhorn, Size distributions of nanoscaled particles and gas temperatures from time-resolved laser-induced-incandescence measurements, Appl. Opt. 42 (2003) 2021–2030. http://www.osapublishing.org/ao/abstract.cfm?URI=ao-42-12-2021

[61] M. Charwath, R. Suntz, H. Bockhorn, Constraints of two-colour TiRe-LII at elevated pressures, Appl. Phys. B 104 (2011) 427–438, doi:10.1007/s00340-011-4432-4.

[62] W. Northrop, S. Bohac, J.-Y. Chin, D. Assanis, Comparison of filter smoke number and elemental carbon mass from partially premixed low temperature combustion in a direct-injection diesel engine, J. Eng. Gas Turbines Power 133 (2011) 102804.

[63] H.A. Michelsen, Understanding and predicting the temporal response of laser-induced incandescence from carbonaceous particles, J. Chem. Phys. 118 (2003) 7012–7045, doi:10.1063/1.1559483.

[64] F.P. Hagen, A. Rinkenburger, J. Günther, H. Bockhorn, R. Niessner, R. Suntz, A. Loukou, D. Trimis, C. Haisch, Spark discharge-generated soot: varying nanostructure and reactivity against oxidation with molecular oxygen by synthesis conditions, J. Aerosol Sci. 143 (2020) 105530, doi:10.1016/j.jaerosci.2020.105530.

[65] P. Muller, Glossary of terms used in physical organic chemistry, Pure Appl. Chem. 66 (1994) 1077–1184.

[66] D. Appel, F.P. Hagen, U. Wagner, T. Koch, H. Bockhorn, D. Trimis, Influence of low ambient temperatures on the exhaust gas and deposit composition of gasoline engines, J. Energy Resour. Technol. 143 (2021) 082306.

[67] F.P. Hagen, P. Vlavakis, H. Bockhorn, R. Suntz, D. Trimis, From molecular to sub-µm scale: the interplay of precursor concentrations, primary particle size, and carbon nanostructure during soot formation in counter-flow diffusion flames, Combust. Flame (2023) accepted, doi:10.1016/j.combustflame.2022.112020.

[68] F.P. Hagen, H. Bockhorn, H. Störmer, A. Loukou, R. Suntz, D. Trimis, Nanostructural and morphological characteristics of single soot aggregates during low-temperature oxidation, Proc. Combust. Inst. 38 (2021) 1153–1161, doi:10.1016/j.proci.2020.06.338.

[69] K. Daun, B. Stagg, F. Liu, G. Smallwood, D. Snelling, Determining aerosol particle size distributions using time-resolved laser-induced incandescence, Appl. Phys. B 87 (2007) 363–372, doi:10.1007/s00340-007-2585-y.

[70] R.L. Vander Wal, T.M. Ticich, A. Brock Stephens, Can soot primary particle size be determined using laser-induced incandescence? Combust. Flame 116 (1999) 291–296, doi:10.1016/S0010-2180(98)00040-6.

[71] J. Zerbs, K.P. Geigle, O. Lammel, J. Hader, R. Stirn, R. Hadef, W. Meier, The influence of wavelength in extinction measurements and beam steering in laser-induced incandescence measurements in sooting flames, Appl. Phys. B 96 (2009) 683–694, doi:10.1007/s00340-009-3550-8.

[72] P. Bielaczyc, A. Szczotka, J. Woodburn, Excess emissions and fuel consumption of modern spark ignition passenger cars at low ambient temperatures, SAE Tech. 2012-01-1070 (2012) 1–10.

[73] H. Badshah, D. Kittelson, W. Northrop, Particle emissions from light-duty vehicles during cold-cold start, SAE Int. J. Engines 9 (2016) 1775–1785.

[74] C. Russo, B. Apicella, A. Tregrossi, A. Ciajolo, K.C. Le, S. Török, P.-E. Bengtsson, Optical band gap analysis of soot and organic carbon in premixed ethylene flames: comparison of in-situ and ex-situ absorption measurements, Carbon 158 (2020) 89–96, doi:10.1016/j.carbon.2019.11.087.

[75] F.J. Bauer, P.A. Braeuer, S. Aßmann, M.A. Thiele, F.J. Huber, S. Will, Characterisation of the transition type in optical band gap analysis of in-flame soot, Combust. Flame 243 (2022) 111986, doi:10.1016/j.combustflame.2022.111986.

[76] K. Tong, B.D. Quay, J.V. Zello, D. Santavicca, Fuel volatility effects on mixture preparation and performance in a GDI engine during cold start, SAE Tech. 2001-01-3650 (2001) 1–20.

[77] J. Yon, R. Lemaire, E. Therssen, P. Desgroux, A. Coppalle, K.F. Ren, Examination of wavelength dependent soot optical properties of diesel and diesel/rapeseed methyl ester mixture by extinction spectra analysis and LII measurements, Appl. Phys. B 104 (2011) 253–271, doi:10.1007/s00340-011-4416-4.

[78] S. Bejaoui, R. Lemaire, P. Desgroux, E. Therssen, Experimental study of the $E(m,\lambda)/E(m,1064)$ ratio as a function of wavelength, fuel type, height above the burner and temperature, Appl. Phys. B 116 (2014) 313–323, doi:10.1007/s00340-013-5692-y.

[79] M. Friedman, The use of ranks to avoid the assumption of normality implicit in the analysis of variance, J. Am. Stat. Assoc. 32 (1937) 675–701.

[80] M. Friedman, A comparison of alternative tests of significance for the problem of $m$ rankings, Ann. Math. Stat. 11 (1940) 86–92.

[81] E. Parzen, On estimation of a probability density function and mode, Ann. Math. Stat. 33 (1962) 1065–1076, doi:10.1214/aoms/1177704472.

[82] W.H. Dalzell, A.F. Sarofim, Optical constants of soot and their application to heat-flux calculations, J. Heat Transf. 91 (1969) 100–104, doi:10.1115/1.3580063.

[83] S. Lee, C. Tien, Optical constants of soot in hydrocarbon flames, Proc. Combust. Inst. 18 (1981) 1159–1166, doi:10.1016/S0082-0784(81)80120-8.

[84] H.-C. Chang, T.T. Charalampopoulos, Determination of the wavelength dependence of refractive indices of flame soot, Proc. R. Soc. A 430 (1990) 577–591, doi:10.1098/rspa.1990.0107.

[85] M. Mannazhi, S. Török, J. Gao, P.-E. Bengtsson, Soot maturity studies in methane-air diffusion flames at elevated pressures using laser-induced incandescence, Proc. Combust. Inst. 38 (2021) 1217–1224, doi:10.1016/j.proci.2020.07.127.

[86] F. Liu, J. Yon, A. Fuentes, P. Lobo, G.J. Smallwood, J.C. Corbin, Review of recent literature on the light absorption properties of black carbon: refractive index,

mass absorption cross section, and absorption function, Aerosol Sci. Technol. 54 (2020) 33–51, doi:10.1080/02786826.2019.1676878.
[87] S. Schraml, C. Heimgärtner, S. Will, A. Leipertz, A. Hemm, Application of a new soot sensor for exhaust emission control based on time resolved laser induced incandescence (TIRE-LII), SAE Int. J. Fuels Lubr. 109 (2000) 2629–2638.
[88] A. Velji, K. Yeom, U. Wagner, U. Spicher, M. Rossbach, R. Suntz, H. Bockhorn, Investigations of the formation and oxidation of soot inside a direct injection spark ignition engine using advanced laser-techniques, SAE Tech. 2010-01-0352 (2010) 1–15.
[89] B. Grob, J. Schmid, N.P. Ivleva, R. Niessner, Conductivity for soot sensing: possibilities and limitations, Anal. Chem. 84 (2012) 3586–3592, doi:10.1021/ac203152z.
[90] D.S. Su, A. Serafino, J.-O. Müller, R.E. Jentoft, R. Schlögl, S. Fiorito, Cytotoxicity and inflammatory potential of soot particles of low-emission diesel engines, Environ. Sci. Technol. 42 (2008) 1761–1765, doi:10.1021/es0716554.